

Chaotic particle dynamics in free-electron lasers

Chiping Chen and Ronald C. Davidson*

Plasma Fusion Center, Massachusetts Institute of Technology, Cambridge, Massachusetts 02139

(Received 27 August 1990)

The motion of a relativistic test electron in a free-electron laser can be altered significantly by the equilibrium self-field effects produced by the beam space charge and current and by the transverse spatial inhomogeneities in a realizable magnetic wiggler field. In a field configuration consisting of an ideal (constant-amplitude) helical-wiggler field and a uniform axial-guide field, it is shown in a model that the inclusion of self-field effects destroys the integrability of the particle equations of motion. Consequently, the group-I orbits and the group-II orbits become chaotic at sufficiently high beam density. An analytical estimate of the threshold value of the self-field parameter $\epsilon_s = \omega_{pb}^2 / c^2 k_w^2$ for the onset of chaos is obtained and found to be in good agreement with computer simulations. In addition, the effects of transverse spatial gradients in a realizable helical-wiggler field with three-dimensional spatial variations are investigated in the absence of an axial-guide field, but including self-field effects. For a thin electron beam ($k_w^2 r_b^2 \ll 1$) and small wiggler field amplitude ($a_w^2 \ll \gamma_b^2$), it is shown that the motion is regular and confined radially provided $\epsilon_a < \gamma_b a_w^2 / (1 + a_w^2)$. However, because of the intrinsic nonintegrability of the motion, the regular region in phase space diminishes in size as the wiggler amplitude is increased. The threshold value of the wiggler amplitude for the onset of chaos is estimated analytically and confirmed by computer simulations for the special case where self-field effects are negligibly small. Moreover, it is shown that the particle motion becomes chaotic on a time scale comparable with the beam transit time through a few wiggler periods.

I. INTRODUCTION

Hamiltonian chaos^{1,2} has been an active area of research in physics and applied sciences. The classic work of Kol'mogorov, Arnol'd, and Moser (KAM) shows that the generic phase space of integrable classical Hamiltonian systems, subject to small perturbations, contains three types of orbits: stable periodic orbits, stable quasi-periodic orbits (KAM tori), and chaotic orbits.³ Unlike three-dimensional, nonintegrable Hamiltonian systems in which different chaotic regions are isolated by the KAM tori, higher-dimensional, nonintegrable Hamiltonian systems exhibit Arnol'd diffusion behavior,⁴ so that chaotic orbits can reach *almost* everywhere in phase space. As the perturbation increases in strength, the KAM tori destabilize and become discrete *fractal* sets. In wave-particle interactions, the breakdown of the last global KAM torus results in stochastic acceleration of particles. An example of such a phenomenon is the stochastic ion heating by a single electrostatic wave in a magnetized plasma.^{5,6}

The purpose of this paper is to investigate chaotic behavior in particle orbits in free-electron lasers (FEL's).⁷⁻⁹ In a free-electron laser, use is made of the unstable interaction of a relativistic electron beam with a transverse wiggler magnetic field to generate coherent electromagnetic waves. An important parameter characterizing FEL operation is the small-signal gain (growth rate). According to linear theory,¹⁰ the gain increases as the beam density and the strength of the wiggler field are increased. However, in the high-current (high-density) regime and the intense wiggler field (strong-pump) regime, the electron orbits can be modified significantly by the equilibri-

um self-fields of the electron beam and the transverse spatial gradients in the applied wiggler field. This raises important questions regarding beam transport and the viability of the free-electron laser interaction process in these regimes.

In the high-current (high-density) regime, the self-electric and self-magnetic fields¹¹ of a non-neutral electron beam are important, and an axial-guide field¹²⁻¹⁴ is often used to provide transverse confinement of the beam electrons. The original one-dimensional calculation by Friedland¹² deals with an integrable system in which the particle orbits are solvable analytically. This treatment neglects self-field effects and the radial dependence of the wiggler field, and yields two classes of stable orbits which are referred to as group-I orbits and group-II orbits.¹⁵ Because the ideal (constant-amplitude) helical-wiggler field $\mathbf{B}_w^{(0)}(z) = -B_w[\mathbf{e}_x \cos(k_w z) + \mathbf{e}_y \sin(k_w z)]$ with $a_w = eB_w / mc^2 k_w = \text{const}$ does not satisfy (exactly) the steady-state vacuum Maxwell equation $\nabla \times \mathbf{B}_w(\mathbf{x}) = 0$, Diamant¹³ and others¹⁶⁻¹⁸ considered a physically realizable helical-wiggler field $\mathbf{B}_w(\mathbf{x})$ with three-dimensional spatial variations and found that (helical) steady-state orbits with guiding center on the axis of the wiggler helix exist for sufficiently small a_w . In contrast to the high-current (high-density) regime, an intense (realizable) wiggler field provides a betatron focusing force so that, in the absence of a uniform axial-guide field, the electron beam can be confined radially in a helical-wiggler field configuration.¹⁹

Earlier investigations of chaos in free-electron lasers have focused on chaotic behavior in particle orbits induced by sideband and radiation fields. Riyopoulos and

Tang²⁰ have analyzed sideband-induced chaos in the electron motion in the field configuration consisting of an ideal helical-wiggler field, the electromagnetic signal wave field, and the sideband wave field. Because the sideband instability^{21,22} is associated with the electrons trapped in the ponderomotive potential, sideband-induced chaos is not likely to affect the free-electron laser interaction until saturation of the signal wave occurs. Chen and Schmidt²³ have shown that the electromagnetic signal wave can also cause chaotic electron motion in the combined helical-wiggler and axial-guide field configuration. Such chaotic behavior occurs on the time scale of the order of many synchrotron periods of an electron trapped in the ponderomotive potential. Like sideband-induced chaos, this effect could be important in free-electron laser oscillators in the nonlinear regime. Recently, Billardon²⁴ has observed evidence of chaotic behavior in the radiation field in a modulated storage-ring FEL.

This paper examines the motion of a relativistic test electron in a helical-wiggler free-electron laser in the absence of electromagnetic signal wave. Of particular interest are the effects of transverse gradients in the beam-produced self-fields and the realizable helical-wiggler field on the dynamics of the test electron. To analyze the self-field effects of an intense electron beam, we consider the particle motion in the combined field configuration consisting of an ideal (constant-amplitude) helical-wiggler field $\mathbf{B}_w^{(0)}(z)$, a uniform axial-guide field $\mathbf{B}_0 = B_0 \mathbf{e}_z$, and the self-electric and self-magnetic fields produced by the space charge and current of the electron beam.²⁵ In the model, the electron beam is assumed to have uniform charge and axial current densities up to radius r_b . By generating Poincaré surface-of-section maps,^{1,3} it is shown that the inclusion of self-field effects destroys the integrability of the motion, and consequently part of phase space becomes chaotic. In particular, the group-I orbits and the group-II orbits become fully chaotic if the self-fields are sufficiently large (which requires sufficiently high beam density). Analysis of the self-field-induced resonances shows that such chaotic behavior originates from the coupling between the guide-field-induced betatron oscillations and the helical motion, modified by the radial gradient of the self-fields. An analytical estimate of the threshold value of the self-field parameter $\epsilon_s = \omega_{pb}^2 / c^2 k_w^2$ for the onset of chaos is obtained and found to be in good agreement with computer simulations. In addition, the characteristic time scale for self-field-induced changes in the particle orbits is shown to be of the order of the time required for a beam electron to transit a few wiggler

periods.

In order to analyze the effects of transverse spatial gradients in a realizable wiggler, we consider particle motion in the field configuration consisting of a realizable (three-dimensional spatial variations) helical-wiggler field and the self-fields of a tenuous electron beam. Because the beam density is low, the particle orbits can be confined radially by the (small) axial component of the helical-wiggler field. A condition for radial confinement of the particle orbits is derived analytically for a thin electron beam ($k_w^2 r_b^2 \ll 1$) and small wiggler amplitude ($a_w^2 / \gamma_b^2 \ll 1$). To demonstrate the existence of chaos, the Poincaré surface-of-section method is used again to examine the phase-space structure in the vicinity of helical orbits with guiding center on the axis of the wiggler helix. In the limit where self-field effects are negligibly small, it is found that the onset of chaos for electron orbits with guiding center on the axis of the wiggler helix occurs whenever the dimensionless parameter $\Delta = a_w / [2(\gamma_b^2 - 1 - a_w^2)]^{1/2}$ exceeds the critical value $\Delta_c(0) = 0.28$, which corresponds to the maximum allowed wiggler amplitude $a_w^c \cong 0.37(\gamma_b^2 - 1)^{1/2}$ for the existence of helical, steady-state orbits for given electron energy γ_b . Furthermore, it is shown that the onset of chaos for off-axis electron orbits occurs at some values of Δ less than $\Delta_c(0)$. This suggests that there is an upper bound on the wiggler field strength for FEL operation.

The organization of this paper is as follows. In Sec. II, a general formulation of the dynamical problem is given in canonical variables. In Sec. III, self-field effects on particle orbits are examined in the applied field configuration consisting of a uniform axial guide field and an ideal helical-wiggler-field. Chaotic behavior is demonstrated by generating Poincaré surface-of-section plots, and an analytical estimate of the threshold value of the self-field parameter is given for the onset of chaos. In Sec. IV, the particle orbits are examined in a realizable helical-wiggler field in the absence of an axial-guide field, but including self-field effects. After deriving an analytical condition for radial confinement of the particle orbits, computer simulations are used to show that the motion is intrinsically nonintegrable and can be chaotic. The condition for onset of chaos is calculated.

II. THEORETICAL MODEL AND ASSUMPTIONS

We consider a relativistic, cylindrical electron beam with radius r_b propagating in the z direction through the externally applied magnetic field configuration

$$\begin{aligned} \mathbf{B}^{\text{ext}}(\mathbf{x}) &= B_0 \mathbf{e}_z + \mathbf{B}_w(\mathbf{x}) \\ &= B_0 \mathbf{e}_z - B_w \{ [I_0(k_w r) \cos(k_w z) + I_2(k_w r) \cos(k_w z - 2\theta)] \mathbf{e}_x \\ &\quad + [I_0(k_w r) \sin(k_w z) - I_2(k_w r) \sin(k_w z - 2\theta)] \mathbf{e}_y - 2I_1(k_w r) \sin(k_w z - \theta) \mathbf{e}_z \} . \end{aligned} \quad (1)$$

Here, $B_0 \mathbf{e}_z$ is the uniform axial-guide field, and $\mathbf{B}_w(\mathbf{x})$ is the realizable helical-wiggler field with amplitude $B_w = \text{const}$ and wiggler wavelength $\lambda_w = 2\pi/k_w = \text{const}$. In Eq. (1), $I_n(x)$ is the modified Bessel functions of the

first kind of order n , $r = (x^2 + y^2)^{1/2}$ is the radial distance from the axis of the helix, and (r, θ) are cylindrical polar coordinates with $x = r \cos \theta$ and $y = r \sin \theta$ (Fig. 1). It is readily shown that the wiggler field defined by Eq. (1)

satisfies the vacuum Maxwell equation $\nabla \times \mathbf{B}_w(\mathbf{x}) = 0$.¹³ In addition, the electron beam is assumed to have uniform density

$$n_b^0(r) = \begin{cases} n_b = \text{const}, & 0 \leq r < r_b \\ 0, & r > r_b, \end{cases} \quad (2)$$

and uniform axial current density $J_{zb}^0(r) = -n_b^0(r)e\beta_{zb}c$ over the radial cross section of the electron beam. Here, $-e$ is the electron charge, c is the speed of light *in vacuo*, and $V_{zb} \equiv \beta_{zb}c = \text{const}$ is the average axial velocity of the electron beam. It is readily shown from the steady-state Maxwell equations that the beam space charge and current generate the self-electric and self-magnetic fields¹¹

$$\mathbf{E}_s = -\frac{m\omega_{pb}^2}{2e}(xe_x + ye_y) \quad (3)$$

and

$$\mathbf{B}_s = \frac{m\omega_{pb}^2\beta_{zb}}{2e}(ye_x - xe_y), \quad (4)$$

in the beam interior ($0 \leq r < r_b$). In Eqs. (3) and (4), m is the electron rest mass, and $\omega_{pb} = (4\pi n_b e^2/m)^{1/2}$ is the nonrelativistic plasma frequency of the beam electrons.

It is the primary purpose of this paper to examine the motion of an individual test electron in the combined applied field configuration and self-fields described by Eqs. (1), (3), and (4). In this regard, it is convenient to represent the equilibrium fields as

$$\mathbf{E}^s(\mathbf{x}) = -\nabla\Phi_s(\mathbf{x}) \quad (5)$$

and

$$\mathbf{B}^{\text{ext}}(\mathbf{x}) + \mathbf{B}^s(\mathbf{x}) = \nabla \times \mathbf{A}(\mathbf{x}), \quad (6)$$

where

$$\Phi_s(\mathbf{x}) = \frac{m\omega_{pb}^2}{4e}(x^2 + y^2) \quad (7)$$

is the electrostatic potential for $0 \leq r < r_b$. In Eq. (6), the total vector potential $\mathbf{A}(\mathbf{x})$ can be expressed as

$$\mathbf{A} = B_0 x e_y + \mathbf{A}_w(\mathbf{x}) + \beta_{zb} \Phi_s(\mathbf{x}) e_z, \quad (8)$$

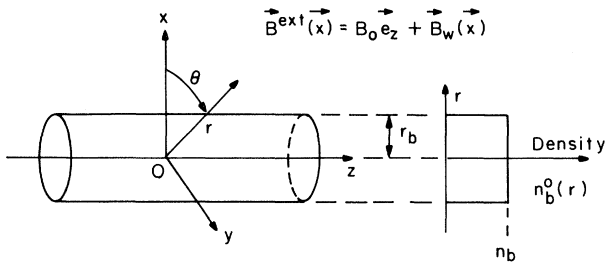


FIG. 1. Schematic of relativistic electron beam and coordinate system. Here, n_b , r_b , and V_{zb} are the density, radius, and average axial velocity of the electron beam, $B_0 e_z$ is the axial-guide field, and $\mathbf{B}_w(\mathbf{x})$ is the transverse wiggler field.

where $\nabla \times (B_0 x e_y) = B_0 e_z$, $\nabla \times [\beta_{zb} \Phi_s(\mathbf{x}) e_z] = \mathbf{B}^s(\mathbf{x})$, and the vector potential for the helical-wiggler field is defined by

$$\mathbf{A}_w(\mathbf{x}) = \frac{mc^2 a_w}{e} \{ [I_0(k_w r) \cos(k_w z) - I_2(k_w r) \cos(k_w z - 2\theta)] e_x + [I_0(k_w r) \sin(k_w z) + I_2(k_w r) \sin(k_w z - 2\theta)] e_y \}. \quad (9)$$

In Eq. (9), $a_w = eB_w/mc^2 k_w$ is the usual dimensionless measure of the wiggler field amplitude.

The equations of motion for a test electron within the beam ($0 \leq r < r_b$) can be derived from the Hamiltonian

$$H = [(c\mathbf{P} + e\mathbf{A})^2 + m^2 c^4]^{1/2} - e\Phi_s \equiv \gamma mc^2 - e\Phi_s. \quad (10)$$

In Eq. (10), \mathbf{P} is the canonical momentum, $\gamma = [1 + (\mathbf{p}/mc)^2]^{1/2}$ is the relativistic mass factor, $\mathbf{p} = \mathbf{P} + e\mathbf{A}/c$ is the mechanical momentum, the electrostatic potential $\Phi_s(\mathbf{x})$ is defined in Eq. (7), and the vector potential $\mathbf{A}(\mathbf{x})$ is defined in Eqs. (8) and (9). Because H is independent of time, the Hamiltonian is a constant of the motion, i.e.,

$$H(x, y, z, P_x, P_y, P_z) = \gamma mc^2 - e\Phi_s = \text{const}, \quad (11)$$

which corresponds to the conservation of total energy (kinetic plus potential energy) of the test electron.

For notational convenience, in the subsequent analysis we introduce the dimensionless potentials $\hat{\mathbf{A}}(\mathbf{x})$ and $\hat{\Phi}_s$, and Hamiltonian \hat{H} defined by

$$\hat{\mathbf{A}} = \frac{e\mathbf{A}(\mathbf{x})}{mc^2}, \quad \hat{\Phi}_s(\mathbf{x}) = \frac{e\Phi_s(\mathbf{x})}{mc^2}, \quad \hat{H} = \frac{H}{mc^2}. \quad (12)$$

In addition, the notation

$$a_0 = \frac{eB_0}{mc^2 k_w} \quad \text{and} \quad a_w = \frac{eB_w}{mc^2 k_w} \quad (13)$$

is introduced, where a_0 is a dimensionless measure of the axial-guide field (B_0), and a_w is a dimensionless measure of the wiggler field amplitude (B_w). Because the electric and magnetic self-fields $\mathbf{E}^s(\mathbf{x})$ and $\mathbf{B}^s(\mathbf{x})$ are proportional to $\omega_{pb}^2 = 4\pi n_b e^2/m$ in the beam interior ($0 \leq r < r_b$), it is also useful to introduce the dimensionless parameter

$$\epsilon_s = \frac{\omega_{pb}^2}{c^2 k_w^2}, \quad (14)$$

which is a measure of the strength of the equilibrium self-fields. Combining Eqs. (12)–(14) with Eqs. (7), (8), and (10) then gives

$$\hat{H} = [(\mathbf{P}/mc + \hat{\mathbf{A}})^2 + 1]^{1/2} - \hat{\Phi}_s, \quad (15)$$

where

$$\hat{\Phi}_s(\mathbf{x}) = \frac{1}{4}\epsilon_s k_w^2 (x^2 + y^2) \quad (16)$$

and

$$\hat{\mathbf{A}}(\mathbf{x}) = a_0 k_w x e_y + \hat{\mathbf{A}}_w(\mathbf{x}) + \beta_{zb} \hat{\Phi}_s(\mathbf{x}) e_z. \quad (17)$$

In Eq. (17), $\hat{\mathbf{A}}_w(\mathbf{x}) = e \mathbf{A}_w(\mathbf{x}) / mc^2$ is the dimensionless vector potential for the helical-wiggler field, and $\mathbf{A}_w(\mathbf{x})$ is defined in Eq. (9). In Secs. III and IV, it is assumed that $k_w^2 r_b^2 < 1$. Therefore, expanding $\hat{\mathbf{A}}_w(\mathbf{x})$ correct to order $a_w k_w^2 r^2$, we obtain (for $r < r_b$)

$$\hat{\mathbf{A}}_w(\mathbf{x}) = \hat{\mathbf{A}}_w^{(0)}(\mathbf{x}) + \hat{\mathbf{A}}_w^{(2)}(\mathbf{x}) + O(a_w k_w^4 r^4). \quad (18)$$

In Eq. (18), $\hat{\mathbf{A}}_w^{(0)}$ is the leading-order vector potential for an ideal helical wiggler, i.e.,

$$\hat{\mathbf{A}}_w^{(0)} = a_w [\mathbf{e}_x \cos(k_w z) + \mathbf{e}_y \sin(k_w z)]. \quad (19)$$

Moreover, $\hat{\mathbf{A}}_w^{(2)}$ represents the correction to Eq. (19) of order $a_w k_w^2 r^2$ defined by

$$\begin{aligned} \hat{\mathbf{A}}_w^{(2)} = \frac{a_w}{8} \{ & [(k_w^2 x^2 + 3k_w^2 y^2) \cos(k_w z) \\ & - 2k_w^2 xy \sin(k_w z)] \mathbf{e}_x \\ & + [(k_w^2 y^2 + 3k_w^2 x^2) \sin(k_w z) \\ & - 2k_w^2 xy \cos(k_w z)] \mathbf{e}_y \}. \end{aligned} \quad (20)$$

From Eqs. (15)–(17), it is clear that there is a large region of the parameter space (a_0, a_w, ϵ_s) in which the motion of an individual test electron can be investigated. The remainder of this paper focuses on the following two cases: (a) in Sec. III, electron motion is investigated for a thin ($k_w^2 r_b^2 \ll 1$) electron beam propagating parallel to a strong axial-guide field ($B_0 \neq 0$ and $a_0 > a_w$); (b) in Sec. IV, electron motion is investigated for a beam propagating through zero axial-guide field ($B_0 = 0$ and $a_0 = 0$) and a strong-focusing wiggler field ($a_w \neq 0$ and $k_w^2 r_b^2 < 1$, but not necessarily $k_w^2 r_b^2 \ll 1$).

In case (a) (Sec. III), the assumption $k_w^2 r_b^2 \ll 1$ corresponds to $|\hat{\mathbf{A}}_w^{(2)}| \ll |\hat{\mathbf{A}}_w^{(0)}|$ [compare Eqs. (19) and (20)]. Therefore, we approximate the vector potential for the wiggler field by the ideal value $\hat{\mathbf{A}}_w = \hat{\mathbf{A}}_w^{(0)} = a_w [\mathbf{e}_x \cos(k_w z) + \mathbf{e}_y \sin(k_w z)]$. Because $a_0 > a_w$ is assumed, the axial magnetic field $B_0 \mathbf{e}_z$ plays an important role in providing radial confinement of the electron orbits in the presence of the (defocusing) space-charge field $\mathbf{E}^s(\mathbf{x})$. Indeed, for the special case where $a_w = 0$, an electron with axial velocity $v_z \cong V_{zb} = \beta_{zb} c$ and small transverse momentum $(p_x^2 + p_y^2)^{1/2} \ll \gamma_{zb} mc$ is radially confined provided¹¹

$$2\gamma_{zb} \epsilon_s (1 - \beta_{zb}^2) < a_0^2, \quad (21)$$

where $\gamma_{zb} = (1 - \beta_{zb}^2)^{-1/2}$, $\epsilon_s = \omega_{pb}^2 / c^2 k_w^2$, and $a_0 = eB_0 / mc^2 k_w \cong \omega_{cz} / ck_w$. Equation (21) is equivalent to the familiar inequality $2\gamma_{zb} \omega_{pb}^2 (1 - \beta_{zb}^2) < \omega_{cz}^2$, required for radial confinement of a non-neutral electron beam by an axial-guide field $B_0 \mathbf{e}_z$.

By contrast, in case (b) (Sec. IV), the axial-guide field is zero ($B_0 = 0$ and $a_0 = 0$), and the defocusing space-charge force associated with $\mathbf{E}^s(\mathbf{x})$ is counteracted by the (focusing) magnetic force associated with the second-order vector potential $\hat{\mathbf{A}}_w^{(2)}$ for the wiggler field defined in Eq. (20). For an electron with axial velocity $v_z \cong V_{zb} = \beta_{zb} c$, perpendicular momentum $(p_x^2 + p_y^2)^{1/2} \cong mca_w$, and total mechanical energy $\gamma \cong \gamma_b = [(1 + a_w^2) / (1 - \beta_{zb}^2)]^{1/2}$

$= \gamma_{zb} (1 + a_w^2)^{1/2}$, it can be shown that the condition for radial confinement of the electron orbits is given by [Eq. (58)]

$$\gamma_b \epsilon_s (1 - \beta_{zb}^2) < a_w^2. \quad (22)$$

Here, $\epsilon_s = \omega_{pb}^2 / c^2 k_w^2$ and $a_w = eB_w / mc^2 k_w \cong \omega_{cw} / ck_w$, and the inequality in Eq. (22) can be expressed in the equivalent form $\gamma_b \omega_{pb}^2 (1 - \beta_{zb}^2) < \omega_{cw}^2$. In Eq. (22), γ_b , β_{zb} , and a_w are related by $1 - \beta_{zb}^2 = (1 + a_w^2) / \gamma_b^2$. For specified beam density n_b , note from Eq. (22) that sufficiently large wiggler amplitude a_w is required for confinement of the electron orbits.

III. PARTICLE ORBITS IN COMBINED AXIAL-GUIDE FIELD AND IDEAL HELICAL-WIGGLER FIELD

We first examine the motion of an individual test electron for the case where $B_0 \neq 0$ and the axial-guide field is sufficiently strong that

$$a_0 > a_w. \quad (23)$$

For a thin electron beam with $k_w^2 r_b^2 \ll 1$, it follows from Eqs. (15)–(20) that the Hamiltonian $\hat{H} = H / mc^2$ can be approximated by (for $r < r_b$)

$$\begin{aligned} \hat{H}(k_w x, k_w y, k_w z, P_x / mc, P_y / mc, P_z / mc) \\ = [(\mathbf{P} / mc + \hat{\mathbf{A}})^2 + 1]^{1/2} - \frac{1}{4} \epsilon_s k_w^2 (x^2 + y^2), \end{aligned} \quad (24)$$

where

$$\begin{aligned} \hat{\mathbf{A}}(\mathbf{x}) = a_0 k_w x \mathbf{e}_y + a_w [\mathbf{e}_x \cos(k_w z) + \mathbf{e}_y \sin(k_w z)] \\ + \frac{1}{4} \beta_{zb} \epsilon_s k_w^2 (x^2 + y^2) \mathbf{e}_z. \end{aligned} \quad (25)$$

Note in Eq. (25) that $\hat{\mathbf{A}}_w(\mathbf{x})$ has been approximated by $\hat{\mathbf{A}}_w^{(0)}(\mathbf{x}) = a_w [\mathbf{e}_x \cos(k_w z) + \mathbf{e}_y \sin(k_w z)]$ for an ideal helical-wiggler field.

A. Hamiltonian in guiding-center variables

As stated in Sec. II, because \hat{H} does not depend explicitly on time t , the total energy $\hat{H} = \gamma - \epsilon_s k_w^2 (x^2 + y^2) / 4$ is a constant of the motion. In order to find an additional constant of the motion and calculate the resonances, it is useful to perform the canonical transformation to the new variables $(\phi, \psi, k_w z', k_w P_\phi / mc, k_w P_\psi / mc, P_z' / mc)$ defined by²⁵

$$\begin{aligned} k_w x = \left[\frac{2}{a_0} \frac{k_w P_\phi}{mc} \right]^{1/2} \sin(\phi + k_w z') \\ - \left[\frac{2}{a_0} \frac{k_w P_\psi}{mc} \right]^{1/2} \cos(\psi - k_w z'), \end{aligned} \quad (26)$$

$$\begin{aligned} k_w y = \left[\frac{2}{a_0} \frac{k_w P_\psi}{mc} \right]^{1/2} \sin(\psi - k_w z') \\ - \left[\frac{2}{a_0} \frac{k_w P_\phi}{mc} \right]^{1/2} \cos(\phi + k_w z'), \end{aligned} \quad (27)$$

$$k_w z = k_w z', \quad (28)$$

$$\frac{P_x}{mc} = \left[2a_0 \frac{k_w P_\phi}{mc} \right]^{1/2} \cos(\phi + k_w z'), \quad (29)$$

$$\frac{P_y}{mc} = \left[2a_0 \frac{k_w P_\psi}{mc} \right]^{1/2} \cos(\psi - k_w z'), \quad (30)$$

$$\frac{P_z}{mc} = \frac{P_{z'}}{mc} - \frac{k_w P_\phi}{mc} + \frac{k_w P_\psi}{mc}, \quad (31)$$

where $a_0 = eB_0/mc^2 k_w$. It is shown later in Sec. III B

[see Eqs. (39)–(41)] that $k_w r_c = (2k_w P_\phi/a_0 mc)^{1/2}$ and $k_w r_g = (2k_w P_\psi/a_0 mc)^{1/2}$ are the normalized gyroradius and guiding-center radius, respectively, of the steady-state orbits. In Eqs. (26)–(31), we introduce the dimensionless variables

$$\hat{P}_\phi = \frac{k_w P_\phi}{mc}, \quad \hat{P}_\psi = \frac{k_w P_\psi}{mc}, \quad \hat{P}_{z'} = \frac{P_{z'}}{mc}. \quad (32)$$

Some straightforward algebra then shows that the Hamiltonian $\hat{H} = H/mc^2$ in the new variables can be expressed as

$$\hat{H}(\phi, \psi, \hat{P}_\phi, \hat{P}_\psi, \hat{P}_{z'}) = [2a_0 \hat{P}_\phi + 2a_w (2a_0 \hat{P}_\phi)^{1/2} \cos\phi + (\hat{P}_{z'} - \hat{P}_\phi + \hat{P}_\psi + \beta_{zb} \hat{\Phi}_s)^2 + a_w^2 + 1]^{1/2} - \hat{\Phi}_s = \text{const.} \quad (33)$$

Here, $a_w = eB_w/mc^2 k_w$, and the normalized self-field potential $\hat{\Phi}_s = e\Phi_s/mc^2$ is defined by

$$\hat{\Phi}_s = \frac{\epsilon_s}{2a_0} [\hat{P}_\phi + \hat{P}_\psi - 2(\hat{P}_\phi \hat{P}_\psi)^{1/2} \sin(\phi + \psi)]. \quad (34)$$

Because \hat{H} in Eq. (33) does not depend explicitly on z' , it follows that $\hat{P}_{z'} = \text{const.}$ Also, note that the analysis presented in this section is restricted to the case of nonzero axial-guide field $B_0 \mathbf{e}_z$. [The canonical transformation in Eqs. (26)–(31) becomes singular in the limit $a_0 = eB_0/mc^2 k_w \rightarrow 0$.]

B. Integrable limit ($\epsilon_s = 0$)

In the limit where self-field effects are negligibly small ($\epsilon_s = 0$ and $\hat{\Phi}_s = 0$), the Hamiltonian in Eq. (33) reduces to

$$\begin{aligned} \hat{H}_0(\phi, \hat{P}_\phi, \hat{P}_\psi, \hat{P}_{z'}) &= [2a_0 \hat{P}_\phi + 2a_w (2a_0 \hat{P}_\phi)^{1/2} \cos\phi \\ &\quad + (\hat{P}_{z'} - \hat{P}_\phi + \hat{P}_\psi)^2 \\ &\quad + a_w^2 + 1]^{1/2} \equiv \gamma_0. \end{aligned} \quad (35)$$

Equation (35) possesses three constants of the motion, namely, \hat{P}_ψ , $\hat{P}_{z'}$, and γ_0 . The motion is integrable and has been analyzed by several authors.^{12,13,15,23} It is readily shown from Eq. (35) that the steady-state orbits ($d\phi/d\tau = 0$ and $d\hat{P}_\phi/d\tau = 0$ with $\tau = ck_w t$) are given by

$$\cos\phi_0 = \pm 1, \quad (36)$$

$$(2a_0 \hat{P}_{\phi 0})^{1/2} = \pm \frac{a_w a_0}{\hat{P}_{z 0} - a_0} > 0, \quad (37)$$

where $\hat{P}_{z 0} = \hat{P}_{z'} - \hat{P}_{\phi 0} + \hat{P}_\psi$ is the normalized axial mechanical momentum. Substituting Eqs. (36) and (37) into Eq. (35) yields

$$\hat{P}_{z 0}^2 \left[1 + \frac{a_w^2}{(\hat{P}_{z 0} - a_0)^2} \right] + 1 = \gamma_0^2, \quad (38)$$

which determines the values of $\hat{P}_{z 0} = p_{z 0}/mc$ in terms of the parameters a_w , a_0 , and γ_0 . Equation (38) is a fourth-order algebraic equation for $\hat{P}_{z 0}$, which has at most four real roots. Figure 2 shows the dependence of $\hat{P}_{z 0}$ on the

strength of the axial-guide field a_0 for the case $a_w = 0.2$ and $\gamma_0 = 3.0$. Here, the solid (dashed) curves represent stable (unstable) orbits, and the dotted line represents the magnetoresonance condition $\hat{p}_{z 0} = a_0$. The stable orbit with $\hat{p}_{z 0} > a_0$ is known as the group-I orbit, whereas the stable orbit with $\hat{p}_{z 0} < a_0$ is known as the group-II orbit. It is clear from Fig. 2 that the group-I orbit exists for a_0 in the range $0 < a_0 < a_0^{\text{cr}}$ and merges with the unstable orbit at $a_0 = a_0^{\text{cr}} \cong 2.1$. In general, the value of a_0^{cr} for the merging of the group-I orbit and the unstable orbit depends on γ_0 and a_w . Substituting $\phi = \phi_0$, $\psi = \psi_0 + \beta_{z 0} \tau$, $k_w z' = k_w z'_0 + \beta_{z 0} \tau$, $\hat{P}_\phi = \hat{P}_{\phi 0}$, and $\hat{P}_\psi = \hat{P}_{\psi 0}$ into Eqs. (26)–(28), it is readily shown that the steady-state trajectories can be expressed in Cartesian coordinates as

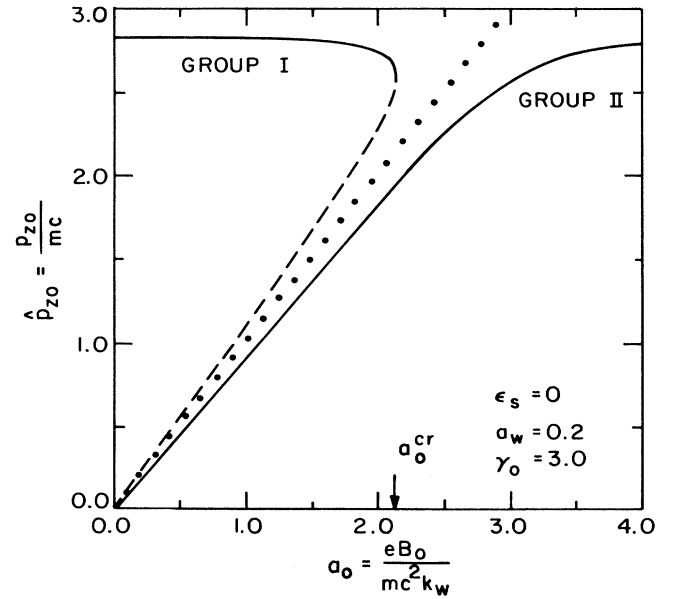


FIG. 2. Plot of the integrable steady-state orbits calculated from Eq. (16) for $\epsilon_s = 0$, $\gamma_0 = 3.0$, and $a_w = 0.2$. The solid (dashed) curves correspond to the stable (unstable) orbits, and the dotted straight line designates the magnetoresonance condition $\hat{p}_z = a_0$.

$$k_w x(\tau) = \pm (2\hat{P}_{\phi 0}/a_0)^{1/2} \sin[k_w z(\tau)] - (2\hat{P}_{\psi 0}/a_0)^{1/2} \cos\psi_0, \quad (39)$$

$$k_w y(\tau) = \mp (2\hat{P}_{\phi 0}/a_0)^{1/2} \cos[k_w z(\tau)] + (2\hat{P}_{\psi 0}/a_0)^{1/2} \sin\psi_0, \quad (40)$$

$$k_w z(\tau) = k_w z_0 + \beta_{z0}\tau, \quad (41)$$

for $\cos\phi_0 = \pm 1$. Here, $\beta_{z0} \equiv \hat{p}_{z0}/\gamma_0$, and $\tau \equiv ck_w t$ is the normalized time variable. Equations (39)–(41) describe helical trajectories with normalized gyroradius $k_w r_c = (2\hat{P}_{\phi 0}/a_0)^{1/2}$ and guiding-center radius $k_w r_g = (2\hat{P}_{\psi 0}/a_0)^{1/2}$.

Figure 3 shows the typical phase-space structure for

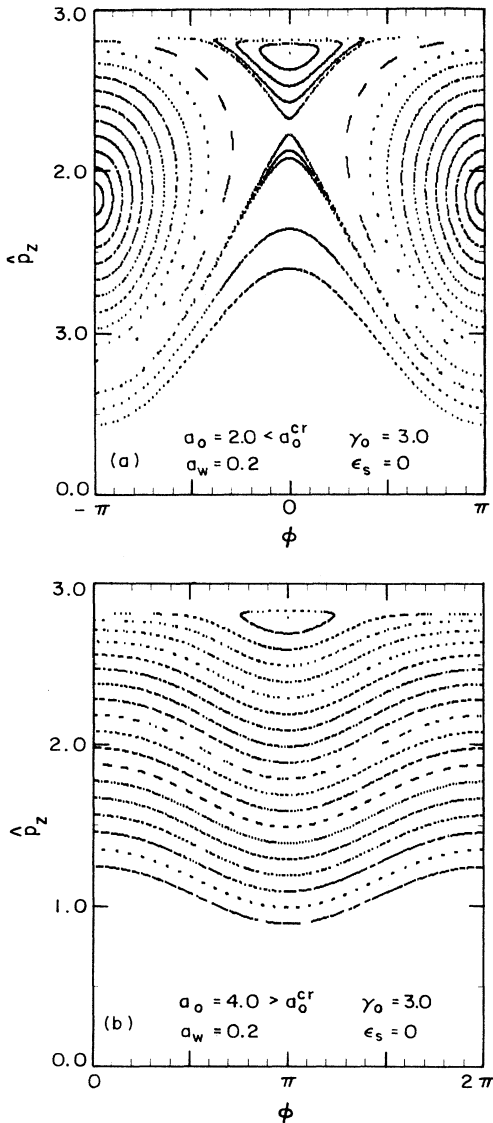


FIG. 3. Contour plots in the integrable phase plane (ϕ, p_z) calculated from Eq. (35) for $\epsilon_s = 0$, $\gamma_0 = 3.0$, and $a_w = 0.2$. The two cases correspond to (a) $a_0 = 2.0 < a_0^{cr} \cong 2.1$ and (b) $a_0 = 4.0 > a_0^{cr}$.

the two cases $0 < a_0 < a_0^{cr}$ and $a_0 > a_0^{cr}$. Here, the elliptic (hyperbolic) fixed points correspond to the stable (unstable) steady-state orbits. The group-I orbit has greater axial momentum than the group-II orbit in Fig. 3(a), whereas only the group-II orbit is allowed in Fig. 3(b). In free-electron laser operation, the electron beam is injected typically into the group-I orbit or the group-II orbit.

An orbit which deviates slightly from the stable (group-I or group-II) orbit, i.e., $|\delta\phi| = |\phi - \phi_0| \ll 1$ and $|\delta\hat{P}_\phi| = |\hat{P}_\phi - \hat{P}_{\phi 0}| \ll 1$, exhibits harmonic, guide-field-induced betatron oscillations. It is straightforward to show from the equations of motion for ϕ and \hat{P}_ϕ that the frequency of the guide-field-induced oscillations is given by²⁵

$$\hat{\omega}_{\beta 0} \equiv \frac{\omega_{\beta 0}}{ck_w} = \frac{|\hat{p}_{z0} - a_0|}{\gamma_0} \left[1 - \frac{a_0}{a_w} \left(\frac{\hat{p}_{t0}}{\hat{p}_{z0}} \right)^3 \right]^{1/2}, \quad (42)$$

where $\hat{p}_{t0} = a_w \hat{p}_{z0} / (\hat{p}_{z0} - a_0)$ is the normalized transverse mechanical momentum. Substituting $\delta\phi(\tau) = \delta\phi_0 \cos(\hat{\omega}_{\beta 0}\tau)$ and $\delta\hat{P}_\phi(\tau) = \delta\hat{P}_{\phi 0} \sin(\hat{\omega}_{\beta 0}\tau)$ into Eqs. (26)–(31), and approximating Eq. (42) by $\hat{\omega}_{\beta 0} \cong |\hat{p}_{z0} - a_0|/\gamma_0$ for $|\hat{p}_{t0}/\hat{p}_{z0}|^3 \ll a_w/a_0$, it is readily shown that the normalized mechanical momentum of an orbit adjacent to the stable, steady-state orbit can be approximated by¹⁵

$$\hat{p}_x(\tau) = \hat{p}_{t0} \cos(\beta_{z0}\tau) + \delta\hat{p}_{t0} \cos(a_0\tau/\gamma_0), \quad (43)$$

$$\hat{p}_y(\tau) = \hat{p}_{t0} \sin(\beta_{z0}\tau) + \delta\hat{p}_{t0} \sin(a_0\tau/\gamma_0), \quad (44)$$

$$\hat{p}_z(\tau) = \hat{p}_{z0} - \delta\hat{p}_{t0} (\hat{p}_{t0}/\hat{p}_{z0}) \cos[(a_0/\gamma_0 - \beta_{z0})\tau], \quad (45)$$

where $\hat{p}_x = p_x/mc$, $\hat{p}_y = p_y/mc$, and $\hat{p}_z = p_z/mc$. Here, $\delta\hat{p}_{t0} = (\hat{p}_{z0} - a_0)\delta\hat{P}_{\phi 0}/a_w$ is the amplitude of the betatron oscillation, and $|\delta\hat{p}_{t0}| \ll |\hat{p}_{t0}|$ is assumed.

C. Chaotic motion ($\epsilon_s \neq 0$)

For $\epsilon_s \neq 0$, the self-field contribution $\hat{\Phi}_s \neq 0$ in Eq. (33) invalidates the constancy of \hat{P}_ψ . The motion described by the Hamiltonian in Eq. (33) occurs in the three-dimensional phase space $(\phi, \psi, \hat{P}_\phi)$, because \hat{P}_ψ is determined from $\hat{H} = \text{const}$. The time scale T_s for self-field-induced changes in the particle orbit can be estimated from the rate of change of the phase $\phi + \psi$ in the electrostatic potential $\hat{\Phi}_s$ defined in Eq. (34). For an electron with $\phi \cong \phi_0$ and $\hat{p}_z \cong \hat{p}_{z0} \cong \beta_{zb}\gamma_b$, because $d(\phi + \psi)/d\tau \cong d\psi/d\tau = \partial\hat{H}/\partial\hat{P}_\psi = \hat{p}_z/\gamma + O(\epsilon_s) \cong \beta_{zb}$ or $d(\phi + \psi)/dt \cong k_w V_b$, the time required for the phase $\phi + \psi$ to advance by 2π is given by

$$T_s = \frac{2\pi}{k_w V_b} = \frac{\lambda_w}{V_b}. \quad (46)$$

Equation (46) is the characteristic time scale for the electron to experience self-field-induced modifications as the electron undergoes the helical motion described by Eqs. (39)–(41). In Eq. (46), $\lambda_w = 2\pi/k_w$ is the wiggler period.

For $\epsilon_s k_w^2 r_b^2 \ll 1$, in the vicinity of the group-I orbits or the group-II orbits, the particle motion occurs on a torus as illustrated in Fig. 4. In Fig. 4, the circular, dashed line represents the orbit $(\phi_0, \hat{P}_{\phi 0})$; the toroidal angle represents

$\psi(\tau)$; the poloidal angle $\alpha(\tau)$ represents the phase of the betatron oscillations $\delta\phi = \phi - \phi_0 = \delta\phi_0 \cos\alpha(\tau)$, and $\delta\hat{P}_\phi = \hat{P}_\phi - \hat{P}_{\phi_0} = \delta\hat{P}_{\phi_0} \sin\alpha(\tau)$; and β_{zb} and $\hat{\omega}_{\beta_0}$ are the normalized angular velocities of the two angles ψ and α , respectively. Clearly, an approximate resonance condition is

$$n\hat{\omega}_{\beta_0} + l\beta_{zb} = 0, \quad (47)$$

where l and n are integers. A detailed resonance analysis has been carried out.²⁵ For example, for $l=1$, it is found that the resonance condition and the resonance width $\hat{\omega}_n$ are given by

$$n \frac{|\hat{p}_{z0} - a_0|}{\gamma_b} \left[1 - \frac{a_0}{a_w} \left(\frac{\hat{p}_{t0}}{\hat{p}_{z0}} \right)^3 \right]^{1/2} + \frac{\hat{p}_{z0}}{\gamma_b} - \frac{\epsilon_s}{2a_0} \left[1 - \beta_{zb} \frac{\hat{p}_{z0}}{\gamma_b} \right] = 0, \quad n=0, \pm 1, \pm 2, \dots, \quad (48)$$

and

$$\hat{\omega}_n = \left[\frac{8\epsilon_s \gamma_b}{a_0} |J_n(\delta\phi_0)| \right]^{1/2} (\hat{P}_{\phi_0} \hat{P}_{\psi_0})^{1/4} = 4 \left[\frac{\gamma_b r_c r_g I_b |J_n(\delta\phi_0)|}{\beta_{zb} r_b^2 I_A} \right]^{1/2}. \quad (49)$$

Here, $\hat{\omega}_n$ is the width of the separatrix of the resonance of order n projected along the \hat{p}_z axis. [For example, for a pendulum described by the Hamiltonian $\hat{H}(\theta, P_\theta) = P_\theta^2/2 - A \cos\theta$, the separatrix width is given by $w = 4A^{1/2}$.] In Eqs. (48) and (49), r_b , I_b , and $\gamma_b mc^2$ are the radius, current, and energy of the electron beam; $I_A = mc^3/e \cong 17$ kA is the Alfvén current; and $r_c = (2\hat{P}_{\phi_0}/k_w^2 a_0)^{1/2}$ and $r_g = (2\hat{P}_{\psi_0}/k_w^2 a_0)^{1/2}$ are the gyroradius and guiding-center radius, respectively. Figure 5 shows plots of the resonance curves (the solid curves) corresponding to the solutions to Eq. (48) for $\epsilon_s = 0.64$, $\gamma_b = \gamma_0 = 3.0$, $a_w = 0.2$, and $n = -1, -2$, and

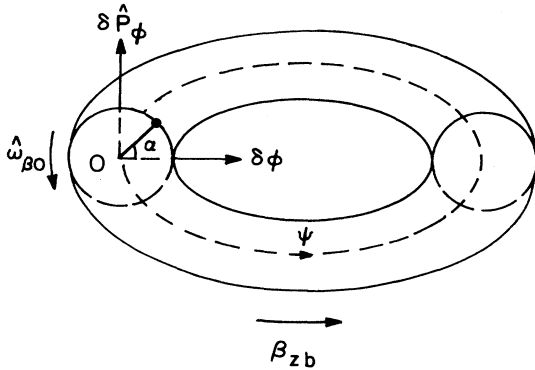


FIG. 4. Schematic of torus in the vicinity of the stable, steady-state orbit $(\phi_0, \hat{P}_{\phi_0})$. Here, β_{zb} and $\hat{\omega}_{\beta_0}$ are the normalized angular velocities of the angle ψ and the phase α of the betatron oscillation, respectively.

–3. The dashed curves in Fig. 5 are the integrable steady-state orbits calculated from Eq. (38). When the resonance curves of order n intersect integrable, stable, steady-state orbits, islands of order n are expected to appear in the vicinity of the steady-state orbits in phase space.

In order to demonstrate that the particle motion is indeed chaotic, Poincaré surface-of-section maps have been generated by numerically integrating the equations of motion derived from the Hamiltonian in Eq. (33). Figure 6 shows nonintegrable surface-of-section plots for $\hat{H} = 3.0$, $a_w = 0.2$, and the two cases (a) $0 < a_0 = 2.0 < a_0^{cr} \cong 2.1$ and $\epsilon_s = 0.16$, and (b) $a_0 = 4.0 > a_0^{cr}$ and $\epsilon_s = 0.64$. The integrable limits corresponding to Figs. 6(a) and 6(b) are shown in Figs. 3(a) and 3(b), respectively, for the case $\epsilon_s = 0$. In Fig. 6, the initial condition for \hat{P}_ψ is fixed at the value $k_w r_g = (2\hat{P}_{\psi_0}/a_0)^{1/2} = 0.25$, whereas the initial condition for \hat{p}_z is allowed to vary. Chaotic orbits are evident in Fig. 6. We also find that it takes (typically) only a few iterations for a chaotic orbit to spread throughout the chaotic region. Because the characteristic time for an iteration of the Poincaré map is approximately $T_s = \lambda_w/V_b$ [Eq. (46)], it follows that chaotic orbits can fill out the chaotic region once the beam passes through a few wiggler periods. The second-order island appearing near the group-II orbit in Fig. 6(b) occurs near the intersection between the $n = -2$ resonance curve and the group-II orbit at $a_0 = 4.0$ in Fig. 5. Note that the self-fields are not intense enough [$\epsilon_s = 0.16$ in Fig. 6(a), and $\epsilon_s = 0.64$ in Fig. 6(b)] to cause high-degree chaos in the vicinity of either the group-I orbit in Fig. 6(a) or the group-II in Fig. 6(b).

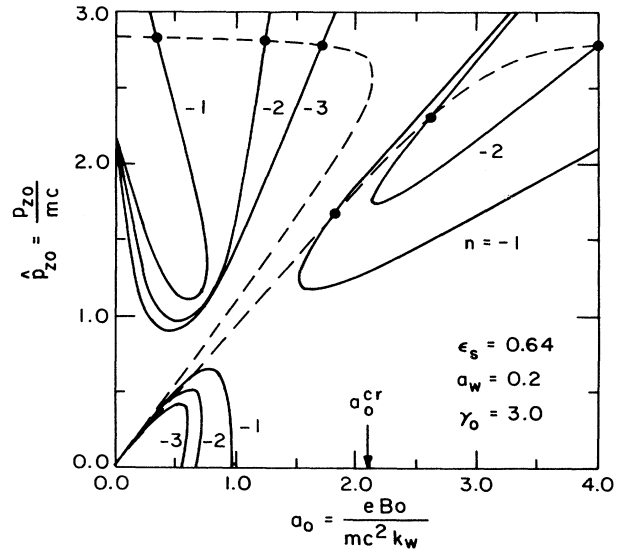


FIG. 5. The equilibrium self-field resonance curves (solid curves) correspond to the solutions to Eq. (48) for $\epsilon_s = 0.64$, $\gamma_0 = 3.0$, $a_w = 0.2$, and $n = -1, -2$, and -3 . The dashed curves are the integrable steady-state orbits calculated in Fig. 2, and the dots mark the intersections between the resonance curves and the steady-state orbits.

The threshold values of the parameter ϵ_s for the onset of chaos can be estimated, using the scaling relation in Eq. (49). The criterion used here is that the onset of chaos occurs whenever the half-width of the self-field-induced resonance near the stable, steady-state orbit is greater than the momentum separation between the resonance and the steady-state orbit. For example, the onset of chaos for the case corresponding to Fig. 6(b) can be estimated by making use of the secondary resonance at $\phi \cong 0.85\pi$ and $\hat{p}_z \cong 2.5$ in Fig. 6(b). Substituting the values $n = -2$, $\delta\phi_0 \cong 0.15\pi$, $\gamma_b = 3.0$, $a_0 = 4.0$, $k_w r_g = (2\hat{P}_{\psi 0}/a_0)^{1/2} = 0.25$, and $k_w r_c = (2\hat{P}_{\phi 0}/a_0)^{1/2}$

$= [a_w/(a_0 - \hat{p}_{z0})]^{1/2} = [0.2/(4.0 - 2.8)]^{1/2} = 0.4$ into Eq. (49), we find that the width of the resonance scales as $\hat{\omega}_{-2} = 0.43\epsilon_s^{1/2}$. Note from Fig. 6(b) that the momentum separation between the group-II orbit and the resonance is $\Delta\hat{p}_z \cong 0.3$. Therefore it follows from $\hat{\omega}_{-2}/2 = \Delta\hat{p}_z$ that the estimated value of ϵ_s for the onset of chaos is given by $\epsilon_s \cong 1.2$. In reality, the actual onset of chaos for the group-II orbit [corresponding to the group-II orbit in Fig. 6(b)] occurs at $\epsilon_s \cong 2.5$ and is shown in Fig. 7, where $a_0 = 4.0$, $\hat{H} = 3.0$, $a_w = 0.2$, $\beta_{zb} = 0.93$, and $k_w r_b = 0.65$. As an example, for $\lambda_w = 3.0$ cm, the dimensionless parameters in Fig. 7 correspond to $r_b = 0.31$ cm, $I_b = 4.3$ kA, $B_w = 710$ G, $B_0 = 14.2$ kG, $\beta_{zb} = 0.93$, and $\gamma_b = 3.0$.

IV. PARTICLE ORBITS IN A REALIZABLE HELICAL-WIGGLER FIELD

In this section, we examine the motion of an individual test electron for the case where the axial-guide field is zero ($B_0 = 0$ and $a_0 = 0$) and the wiggler magnetic field is described by a realizable helical wiggler. For an electron beam with $k_w^2 r_b^2 < 1$, it follows from Eqs. (15)–(20) that the Hamiltonian $\hat{H} = H/mc^2$ can be approximated by (for $r < r_b$)

$$\hat{H}(k_w x, k_w y, k_w z, \hat{P}_x, \hat{P}_y, \hat{P}_z) = [(\hat{\mathbf{P}} + \hat{\mathbf{A}})^2 + 1]^{1/2} - \frac{1}{4}\epsilon_s k_w^2 (x^2 + y^2). \quad (50)$$

Here, $\hat{\mathbf{P}} = \mathbf{P}/mc$ is the normalized canonical momentum, and the dimensionless vector potential is defined by

$$\hat{\mathbf{A}}(\mathbf{x}) = \hat{\mathbf{A}}_w^{(0)}(\mathbf{x}) + \hat{\mathbf{A}}_w^{(2)}(\mathbf{x}) + \frac{1}{4}\beta_{zb}\epsilon_s k_w^2 (x^2 + y^2)\mathbf{e}_z. \quad (51)$$

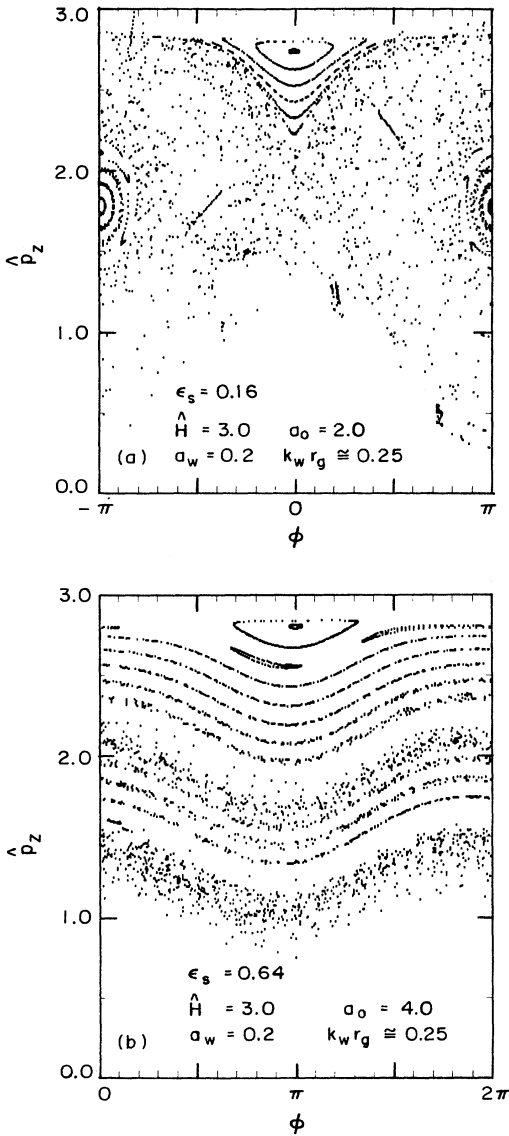


FIG. 6. Typical nonintegrable surface-of-section plots in the (ϕ, \hat{p}_z) plane at $\psi = 0 \pmod{2\pi}$ for the two cases: (a) $0 < a_0 = 2.0 < a_0^{cr} \cong 2.1$ and (b) $a_0 = 4.0 > a_0^{cr}$. Other system parameters are (a) $\epsilon_s = 0.16$, $\hat{H} = 3.0$, $a_w = 0.2$, and $\beta_{zb} = 0.91$, and (b) $\epsilon_s = 0.64$, $\hat{H} = 3.0$, $a_w = 0.2$, and $\beta_{zb} = 0.93$.

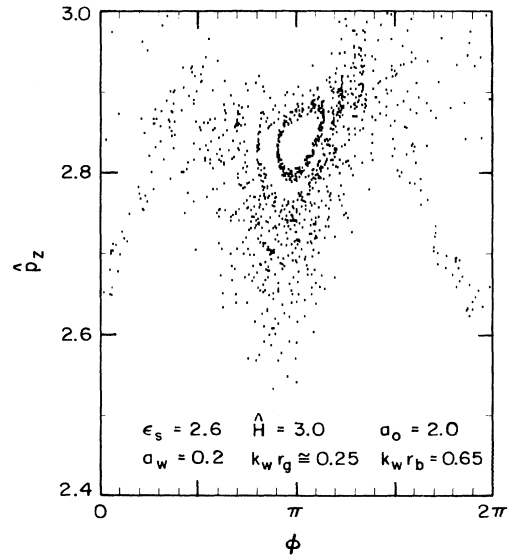


FIG. 7. Surface-of-section plot at the onset of chaos in the group-II orbit for the choice of system parameters $\epsilon_s = 2.5$, $a_0 = 4.0$, $\hat{H} = 3.0$, $a_w = 0.2$, and $\beta_{zb} = 0.93$, corresponding to Fig. 6(b). Here, the normalized effective gyroradius $k_w r_c \cong (2\hat{P}_{\psi 0}/a_0)^{1/2}$ ranges from 0.17 to 0.35, the normalized guiding-center radius is $k_w r_g \cong (2\hat{P}_{\psi 0}/a_0)^{1/2} \cong 0.25$, and the normalized beam radius is $k_w r_b = 0.65$.

In Eq. (51), we have approximated $\hat{\mathbf{A}}_w(\mathbf{x}) \cong \hat{\mathbf{A}}_w^{(0)}(\mathbf{x}) + \hat{\mathbf{A}}_w^{(2)}(\mathbf{x})$ for a realizable helical-wiggler field, and $\hat{\mathbf{A}}_w^{(0)}(\mathbf{x})$ and $\hat{\mathbf{A}}_w^{(2)}(\mathbf{x})$ are defined in Eqs. (19) and (20).

A. Condition for radial orbit confinement

We first consider the case of a thin electron beam with $k_w^2 r_b^2 \ll 1$. Because $\hat{P}_x^2 + \hat{P}_y^2 < k_w^2 r_b^2 a_w^2$ [see Eq. (62)], the Hamiltonian defined in Eqs. (50) and (51) can be expanded to order $k_w^2 r^2$. For $r < r_b$, this yields

$$\hat{H} \cong \hat{H}_0 + \hat{H}_1, \quad (52)$$

where

$$\begin{aligned} \hat{H}_0(k_w z, \hat{P}_x, \hat{P}_y, \hat{P}_z) \\ = \{ \hat{P}_z^2 + 2a_w [\hat{P}_x \cos(k_w z) + \hat{P}_y \sin(k_w z)] + a_w^2 + 1 \}^{1/2} \\ \equiv \gamma_0 \end{aligned} \quad (53)$$

and

$$\begin{aligned} \hat{H}_1 = \frac{1}{2\gamma_0} (\hat{P}_x^2 + \hat{P}_y^2 + 2\hat{\mathbf{A}}_w^{(0)} \cdot \hat{\mathbf{A}}_w^{(2)}) \\ - \frac{\epsilon_s}{4} \left[1 - \beta_{zb} \frac{\hat{P}_z}{\gamma_0} \right] k_w^2 (x^2 + y^2). \end{aligned} \quad (54)$$

For the case of zero transverse canonical momentum with $\hat{P}_x = \hat{P}_y = 0$, it follows from Eq. (53) that the lowest-order (helical) particle orbit is described by

$$\begin{aligned} x_0(\tau) &= r_c \sin[k_w z_0(\tau)] + x_g, \\ y_0(\tau) &= -r_c \cos[k_w z_0(\tau)] + y_g, \\ z_0(\tau) &= (\beta_{z0}/k_w)\tau + z_0(0). \end{aligned} \quad (55)$$

In Eq. (55), $\tau = ck_w t$, $\beta_{z0} = [1 - (1 + a_w^2)/\gamma_0^2]^{1/2} = \text{const}$, $r_c = a_w/k_w \gamma_0 \beta_{z0}$ is the radius of the helical orbit, and x_g and y_g are slow variables describing the center of the helix which is referred to as the guiding center in the remainder of this paper. (Because the center of the helix does not necessarily follow magnetic field lines, the guiding center here is not the one used usually in plasma physics.) Note from $r_c < r_b$ that the assumption $k_w^2 r_b^2 \ll 1$ requires $a_w^2 \ll \gamma_0^2 \beta_{z0}^2$.

To calculate the guiding-center trajectories, we substitute Eqs. (19), (20), and (55) in Eq. (54) and average over τ for one period $2\pi/\beta_{z0}$. For $\gamma_0 \cong \gamma_b$ and $\beta_{z0} \cong \beta_{zb} = [1 - (1 + a_w^2)/\gamma_b^2]^{1/2}$, some straightforward algebra shows that the average Hamiltonian can be expressed as

$$\begin{aligned} \langle \hat{H}_1 \rangle = \frac{1}{2\gamma_b} \left[\hat{P}_x^2 + \hat{P}_y^2 + \gamma_b^2 \hat{\omega}_{\beta w}^2 \left[1 - \frac{\gamma_b \epsilon_s}{a_w^2} (1 - \beta_{zb}^2) \right] \right. \\ \left. \times k_w^2 (x^2 + y^2) \right] + \text{const}, \end{aligned} \quad (56)$$

where

$$\hat{\omega}_{\beta w} \equiv \frac{\omega_{\beta w}}{ck_w} = \frac{a_w}{\sqrt{2}\gamma_b} \quad (57)$$

is the normalized frequency of the wiggler-field-induced betatron oscillations in the absence of self-fields. It follows from Eq. (56) that the guiding center of helical orbit oscillates harmonically about $r=0$ provided $\gamma_b \epsilon_s (1 - \beta_{zb}^2) < a_w^2$, and diverges radially if $\gamma_b \epsilon_s (1 - \beta_{zb}^2) > a_w^2$. Therefore the condition for radial confinement of the particle orbits can be expressed as

$$\gamma_b \epsilon_s (1 - \beta_{zb}^2) < a_w^2, \quad (58)$$

or equivalently,

$$\gamma_b \omega_{pb}^2 (1 - \beta_{zb}^2) < \omega_{cw}^2. \quad (59)$$

Here, $\omega_{pb} = (4\pi e^2 n_b / m)^{1/2}$ is the nonrelativistic plasma frequency, and $\omega_{cw} = eB_w / mc = ck_w a_w$ is the nonrelativistic cyclotron frequency associated with the wiggler field amplitude B_w . Note that the condition in Eqs. (58) and (59) is analogous to the condition for radial confinement of particle orbits in a non-neutral electron beam by a uniform axial magnetic field.¹¹ Expressing $\epsilon_s = \omega_{pb}^2 / c^2 k_w^2 = (4/\beta_{zb} k_w^2 r_b^2)(I_b / I_A)$, where I_b is the beam current and $I_A \equiv mc^3 / e \cong 17$ kA is the Alfvén current, it readily follows that the condition in Eqs. (58) and (59) can be expressed in the equivalent form

$$I_b < I_b^{\text{cr}} \equiv \frac{\gamma_b \beta_{zb} k_w^2 r_b^2}{4} \frac{a_w^2}{1 + a_w^2} I_A. \quad (60)$$

As an example, for $a_w = 0.4$, $k_w r_b = 0.2$, $\gamma_b = 3.0$, and $\beta_{zb} = [1 - (1 + a_w^2)/\gamma_b^2]^{1/2} = 0.93$, the critical value of beam current defined in Eq. (60) is $I_b^{\text{cr}} = 65$ A.

Solving the equations of motion determined from $\langle \hat{H}_1 \rangle$ in Eq. (56) for radially confined orbits, we find that the guiding-center trajectories are given by $x_g(\tau) = x_m \cos(\hat{\omega}_{\beta w}^s \tau + \alpha_x)$ and $y_g(\tau) = y_m \cos(\hat{\omega}_{\beta w}^s \tau + \alpha_y)$. Here, α_x and α_y are the phases of the betatron oscillations, x_m and y_m are the amplitudes, and

$$\hat{\omega}_{\beta w}^s = \hat{\omega}_{\beta w} \left[1 - \frac{\gamma_b \epsilon_s}{a_w^2} (1 - \beta_{zb}^2) \right]^{1/2} \quad (61)$$

is the normalized frequency of the wiggler-field-induced betatron oscillations including self-field effects. Because $\hat{P}_x = \gamma_0 d(k_w x_g) / d\tau$, $\hat{P}_y = \gamma_0 d(k_w y_g) / d\tau$, and $x_m^2 + y_m^2 < r_b^2$, it is readily shown that

$$\hat{P}_x^2 + \hat{P}_y^2 < k_w^2 r_b^2 a_w^2, \quad (62)$$

which assures the validity of the expansion in Eq. (52).

Figure 8 shows typical transverse trajectories for the two cases (a) $\epsilon_s < \epsilon_s^{\text{cr}} \equiv a_w^2 / \gamma_b (1 - \beta_{zb}^2) = \gamma_b a_w^2 / (1 + a_w^2)$, and (b) $\epsilon_s > \epsilon_s^{\text{cr}}$. The orbits in Fig. 8 are obtained by integrating numerically the equations of motion derived from the Hamiltonian defined in Eqs. (50) and (51). In Fig. 8(a), because the focusing force due to the wiggler and self-magnetic fields is greater than the defocusing force of the self-electric field ($\epsilon_s < \epsilon_s^{\text{cr}}$), the guiding center of the orbit oscillates about the axis of the wiggler helix, corresponding to a real value of $\hat{\omega}_{\beta w}^s$. In Fig. 8(b), because the defocusing force exceeds the focusing force

($\epsilon_s > \epsilon_s^{\text{cr}}$), the radius of the guiding center of the orbit oscillates between some minimum radius r_{min} and maximum radius r_{max} . The focusing force provided by higher-order terms in the vector potential expansion in Eq. (18), which become increasingly large as r increases, prevents the particle orbits from diverging indefinitely in the radial direction in Fig. 8(b). Figure 9 shows the plots of the parameter $\epsilon_s^{\text{cr}}/\gamma_b$ versus a_w . Here, the solid curve corresponds to the analytical estimate $\epsilon_s^{\text{cr}}/\gamma_b = a_w^2/(1+a_w^2)$, and the dashed curves are obtained from numerical integration of the equations of motion. In Fig. 9, the two dashed curves correspond to $\gamma_b = 4$ and 10 used in the simulations. It is evident from Fig. 9 that the analytical and numerical results are in good agreement.

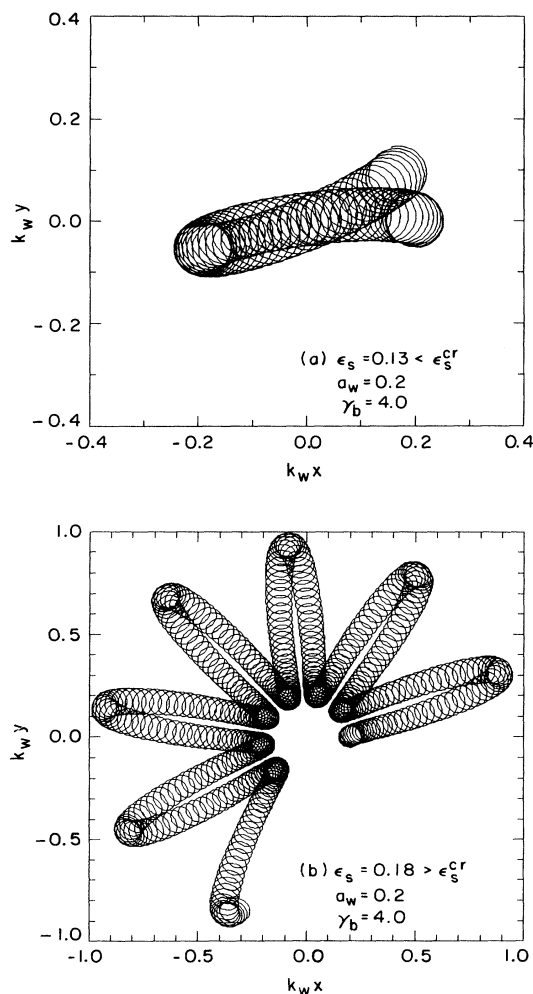


FIG. 8. Plots of typical transverse trajectories for the two cases (a) $\epsilon_s < \epsilon_s^{\text{cr}} \equiv \gamma_b a_w^2 / (1 + a_w^2)$ and (b) $\epsilon_s > \epsilon_s^{\text{cr}}$. Here, the choices of the system parameters for the two cases are (a) $\epsilon_s = 0.13$, $a_w = 0.2$, $\gamma_b = 4.0$, and $\epsilon_s^{\text{cr}} = 0.154$, and (b) $\epsilon_s = 0.18$, $a_w = 0.2$, $\gamma_b = 4.0$, and $\epsilon_s^{\text{cr}} = 0.154$.

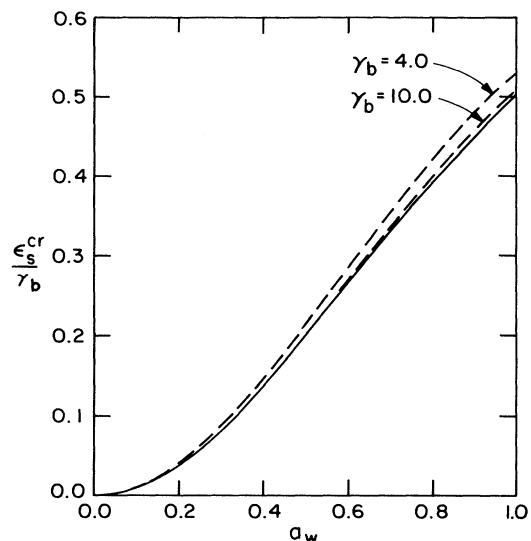


FIG. 9. Plots of $\epsilon_s^{\text{cr}}/\gamma_b$ vs a_w . Here, the solid curve corresponds to the analytical estimate $\epsilon_s^{\text{cr}}/\gamma_b = a_w^2/(1+a_w^2)$, and the dashed curves are obtained by solving numerically the equations of motion for $\gamma_b = 4$ and $\gamma_b = 10$.

B. Chaotic motion in the strong-pump regime

We now examine the particle orbits in the regime where the wiggler field amplitude a_w is sufficiently large that

$$a_w \sim \gamma_b \beta_{zb}. \quad (63)$$

Because the normalized beam radius $k_w r_b$ and gyroradius $k_w r_c = a_w / \gamma_b \beta_{zb}$ are allowed to be of order unity, the analytical treatment in Sec. IV A is no longer valid. For $k_w r \leq k_w r_b < 1$, however, the approximate Hamiltonian defined in Eqs. (50) and (51) still provides an adequate description of the particle motion. In the remainder of this section, we show that the motion is nonintegrable and exhibits chaotic behavior when a_w is sufficiently large.

To simplify the analysis, we assume that self-field effects are negligibly small ($\epsilon_s = 0$ and $\Phi_s = 0$), and focus on the region of the phase space in the vicinity of helical orbits with guiding center on the z axis ($r_g = 0$), electron energy $\gamma = \gamma_b$, and normalized axial velocity $\beta_z \cong \beta_{zb} = [1 - (1 + a_w^2)/\gamma_b^2]^{1/2}$. In addition, it is useful to introduce the dimensionless parameter

$$\Delta \equiv \frac{\omega_{\beta w}}{c k_w \beta_{zb}} = \frac{a_w}{[2(\gamma_b^2 - 1 - a_w^2)]^{1/2}}, \quad (64)$$

which is a measure of the nonintegrability of the motion. Physically, λ_w / Δ is the axial distance through which an electron with energy $\gamma = \gamma_b$ and axial velocity $v_z = \beta_{zb} c$ travels in one betatron oscillation period $2\pi / \omega_{\beta w}$.

For present purposes, it is convenient to describe the particle motion in cylindrical polar coordinates (r, θ, z) . The Hamiltonian in Eq. (50) can be expressed as

$$\hat{H} = \left\{ \left[\hat{P}_r + a_w \left[1 + \frac{k_w^2 r^2}{8} \right] \cos(\theta - k_w z) \right]^2 + \left[\frac{\hat{P}_\theta}{k_w r} - a_w \left[1 + \frac{3k_w^2 r^2}{8} \right] \sin(\theta - k_w z) \right]^2 + \hat{P}_z^2 + 1 \right\}^{1/2}, \quad (65)$$

where the dimensionless variables

$$\hat{P}_r = \frac{P_r}{mc} \quad \text{and} \quad \hat{P}_\theta = \frac{k_w P_\theta}{mc} \quad (66)$$

have been introduced. Because the combination $\theta - k_w z$ appears in \hat{H} , it is useful to perform the canonical transformation to the new variables $(k_w r, \chi, k_w z', \hat{P}_r, \hat{P}_\chi, \hat{P}_{z'})$ defined by

$$\chi = \theta - k_w z, \quad k_w z' = k_w z, \quad (67)$$

$$\hat{P}_\chi = \hat{P}_\theta, \quad \hat{P}_{z'} = \hat{P}_z + \hat{P}_\theta. \quad (68)$$

Here, the generating function is given by $F_2(k_w z, \theta; \hat{P}_{z'}, \hat{P}_\chi) = k_w z \hat{P}_{z'} + (\theta - k_w z) \hat{P}_\chi$. The Hamiltonian in the new variables can be expressed as

$$\hat{H}(k_w r, \chi, \hat{P}_r, \hat{P}_\chi, \hat{P}_{z'} = \text{const}) = \left\{ \left[\hat{P}_r + a_w \left[1 + \frac{k_w^2 r^2}{8} \right] \cos\chi \right]^2 + \left[\frac{\hat{P}_\chi}{k_w r} - a_w \left[1 + \frac{3k_w^2 r^2}{8} \right] \sin\chi \right]^2 + (\hat{P}_{z'} - \hat{P}_\chi)^2 + 1 \right\}^{1/2} = \text{const}. \quad (69)$$

Equation (69) possesses two constants of the motion, namely, \hat{H} and $\hat{P}_{z'}$. The motion occurs in the three-dimensional phase space $(\chi, \hat{P}_\chi, \hat{P}_r)$, because $k_w r$ can be determined from $\hat{H} = \text{const}$.

The (helical) steady-state orbits with guiding center on the z axis are the solutions of the steady-state equations of motion derived from the Hamiltonian in Eq. (69). Following Diament,¹³ it can be shown for $0 \leq \Delta < 0.28$ (Appendix) that the steady-state orbits with normalized axial momentum $\hat{P}_{z'} = \hat{P}_z - \hat{P}_\chi > 0$ are given by

$$\begin{aligned} k_w r &= k_w r_0, \quad \chi = \chi_0 = 3\pi/2, \\ \hat{P}_r &= \hat{P}_{r_0} = 0, \quad \hat{P}_\chi = (3a_w/4)(k_w r_0)^3, \end{aligned} \quad (70)$$

where the normalized gyroradii $k_w r_0 = k_w r_0^<$ and $k_w r_0 = k_w r_0^>$ are the solutions of the algebraic equation¹³

$$f(k_w r_0) \equiv \left[2 \left[1 + \frac{1}{k_w^2 r_0^2} \right] \left[1 + \frac{9k_w^2 r_0^2}{8} \right]^2 - 2 \right]^{-1/2} = \Delta. \quad (71)$$

Because the function $f(k_w r_0)$ satisfies $f(0) = f(\infty) = 0$ and has a (single) maximum $f_m \cong 0.28$ at $k_w r_0 \cong 0.625$, it follows that Eq. (71) has two real solutions when Δ is in the interval $0 \leq \Delta < f_m$, and no real solution otherwise.

Poincaré surface-of-section maps are generated to demonstrate the existence of chaos in the phase space in the vicinity of the steady-state orbit in Eq. (70) with $k_w r_0 = k_w r_0^<$, where $r_0^<$ is the smaller of the two solutions to Eq. (71). Figure 10 shows the Poincaré surface-of-section plots in the (χ, \hat{P}_χ) plane at $\hat{P}_r = 0$ for $\hat{H} = \gamma_b = 6.0$ and $\epsilon_s = 0$, corresponding to the two cases (a) $\Delta = 0.18 < f_m \cong 0.28$ (or $a_w = 1.5$) and (b) $\Delta = 0.22 < f_m$ (or $a_w = 1.8$). The orbits in Fig. 10 are calculated numerically from the equations of motion derived

from the Hamiltonian in Eq. (69). Because $\hat{P}_\chi = -(\hat{P}_z - \hat{P}_{z'})$ [Eq. (68)], a reversal of the vertical axis in Fig. 10 corresponds to the normalized axial momentum $\hat{P}_{z'}$ relative to the constant $\hat{P}_{z'}$. It is evident that the phase space contains regular and chaotic orbits. In fact, the axial velocity of a chaotic orbit can be negative at random time intervals even though the initial axial velocity is positive. In Fig. 10, the fixed point at $\chi = \chi_0 = 3\pi/2$ and $\hat{P}_\chi = \hat{P}_{\chi_0}$ corresponds to the steady-state orbit defined in Eq. (70). Each contour in Fig. 10 corresponds to an orbit with guiding center oscillating about $r = 0$ approximately at the betatron frequency $\omega_{\beta w}$. As the contour size increases, the amplitude of the betatron oscillation increases, and consequently the coupling between the helical motion and the betatron oscillation is enhanced, leading to chaos. Furthermore, as the value of the parameter Δ (or a_w) is increased, the area of the regular region in the phase plane decreases [compare Fig. 10(b) with Fig. 10(a)]. Therefore it is of interest to calculate the threshold value of the parameter $\Delta = \Delta_c(k_w r_{gm})$ for the onset of chaos for an electron orbit with maximum normalized guiding-center radius $k_w r_{gm}$ from the axis of the wiggler helix ($r = 0$). For electron orbits with guiding center on the axis of the wiggler helix, we find that the threshold value is given by

$$\Delta_c(0) = f_m \cong 0.28. \quad (72)$$

Figure 11 shows the dependence of Δ_c on $k_w r_{gm}$, as obtained from the computer simulations. It is found that the function $\Delta_c(k_w r_{gm})$ is independent of the value of the electron energy γ_b . In Fig. 11, although Δ_c decreases monotonically in a weak manner as $k_w r_{gm}$ varies from 0 to 0.5, there is a discontinuous drop in Δ_c at $k_w r_{gm} \cong 0.5$. This may be associated with changes in the resonance structures in phase space. Solving for $a_w = a_w^c$ from Eq. (64) with $\Delta = \Delta_c(0) = 0.28$, it readily follows that the

threshold value of the dimensionless wiggler amplitude for the onset of fully developed chaos is given by

$$a_w^c = 0.37(\gamma_b^2 - 1)^{1/2}. \quad (73)$$

For a given γ_b , the phase space is fully chaotic if $a_w > a_w^c(\gamma_b)$, whereas there is a regular region with some finite area in phase space if $a_w < a_w^c(\gamma_b)$.

Although the present results are similar to the results²⁶ obtained earlier for the case of realizable planar-wiggler field configuration, there are qualitative and quantitative

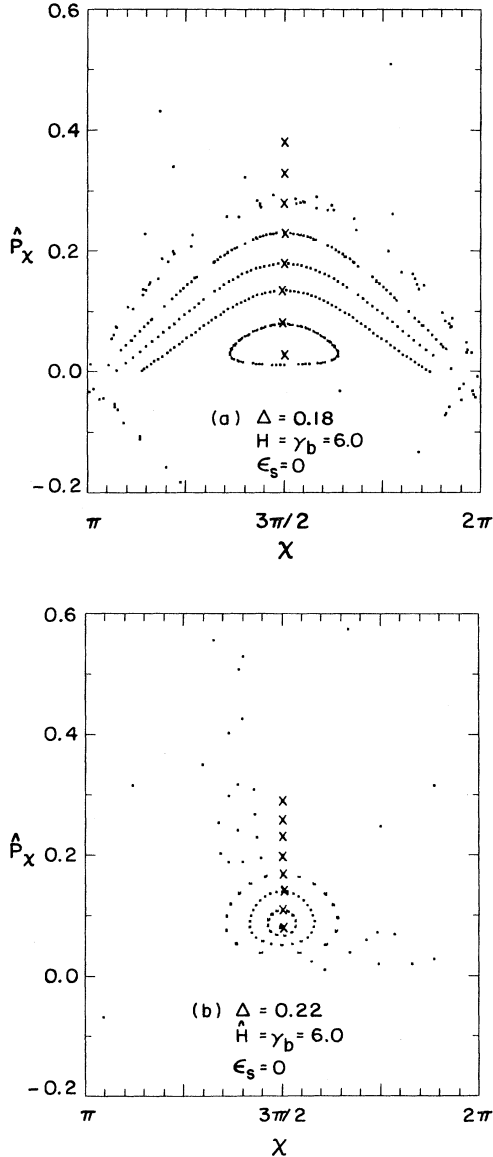


FIG. 10. Poincaré surface-of-section plots in the (χ, \hat{P}_χ) plane at $\hat{P}_r = 0$. Here, 50 iterations are plotted for each orbit with the initial conditions marked by the crosses. The choices of system parameters for the two cases are (a) $\Delta = 0.18$ ($a_w = 1.5$), $\hat{H} = \gamma_b = 6.0$, and $\epsilon_s = 0$, and (b) $\Delta = 0.22$ ($a_w = 1.8$), $\hat{H} = \gamma_b = 6.0$, and $\epsilon_s = 0$.

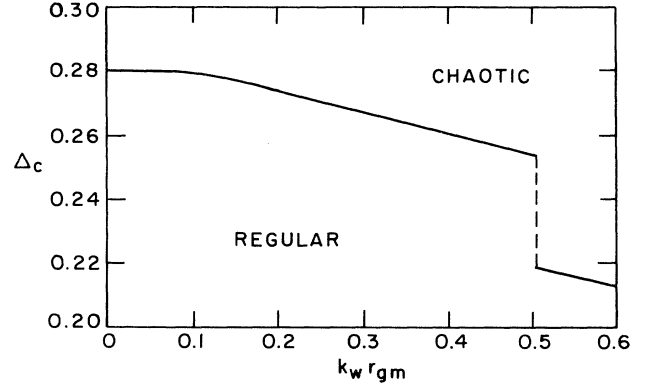


FIG. 11. Plots of Δ_c vs $k_w r_{gm}$ for the onset of chaos in electron orbits with maximum guiding-center radius r_{gm} , as obtained from the computer simulations. The value of $\Delta_c = \Delta_c(k_w r_{gm})$ is found to be independent of the electron energy γ_b , for values of γ_b up to 100.

differences. First, there is a threshold wiggler amplitude $a_w = a_w^c$ beyond which orbits with $r_g = 0$ become unstable and chaotic in the helical-wiggler case, while in the planar-wiggler case, orbits with exactly zero displacement in the wiggler plane are integrable. Second, the threshold value of the wiggler amplitude for the onset of chaos in the helical-wiggler case is less than the corresponding value in the planar-wiggler case, for similar beam radius and energy, and wiggler period.

V. CONCLUSIONS

We have investigated the effects of the equilibrium self-fields and an inhomogeneous wiggler field on the dynamics of a test electron in a helical-wiggler free-electron laser in the absence of electromagnetic signal wave. It was shown that the transverse spatial gradients in the self-fields and a realizable helical-wiggler field can cause chaos in the particle orbits. In addition, the characteristic time scale for radial-gradient-induced changes in the particle orbits is of the order of the beam transit time through a few wiggler periods. The following is a brief summary of the principal results and conclusions.

First, the influence of equilibrium self-fields on the particle orbits was analyzed in the field configuration consisting of an ideal helical-wiggler field and a uniform axial-guide field. It was shown that the inclusion of the equilibrium self-field effects destroys the integrability of the motion, and results in chaotic particle motion at sufficiently high beam density. In particular, the group-I orbits and the group-II orbits can become fully chaotic. The origin of this chaotic behavior is the coupling between the guide-field-induced betatron oscillations and the helical motion, modified by the radial gradient of the self-fields. An analysis of the self-field-induced resonances was carried out, and scaling relations for the resonance widths were derived. Good agreement was found between the computer simulations and the analytical esti-

mate of the threshold value of the self-field parameter for the onset of chaos.

Second, the effects of wiggler-induced betatron oscillations on the particle orbits were analyzed for a realizable helical-wiggler field configuration in the absence of axial-guide field, but including the influence of equilibrium self-fields. For a thin electron beam and small wiggler amplitude, a condition for radial confinement of the particle orbits was derived analytically and verified in computer simulations. Although the particle orbits consist of well-defined helical motion and betatron oscillations when the wiggler amplitude is small, it was shown that the particle trajectories become strongly chaotic when the wiggler amplitude is sufficiently large. As the wiggler amplitude is increased, the area of the regular region in phase space decreases in the Poincaré surface-of-section plots. For the special case where self-field effects are negligibly small, the threshold value of the wiggler amplitude for the onset of fully developed chaos was found to

be $a_w^c \cong 0.37(\gamma_b^2 - 1)^{1/2}$, which corresponds to the maximum allowed value of the wiggler amplitude for the existence of regular helical orbits for given electron energy γ_b .

ACKNOWLEDGMENTS

This work was supported in part by the Department of Energy High Energy Physics Division, the Office of Naval Research, and the Naval Research Laboratory Plasma Physics Division. The authors wish to thank Jonathan S. Wurtele for helpful comments on the manuscript.

APPENDIX: ANALYSIS OF STEADY-STATE ORBITS

The equations of motion derived from the Hamiltonian in Eq. (69) have the form

$$\frac{d(k_w r)}{d\tau} = \frac{\partial \hat{H}}{\partial \hat{P}_r} = \frac{1}{\gamma} \left[\hat{P}_r + a_w \left[1 + \frac{k_w^2 r^2}{8} \right] \cos \chi \right], \quad (\text{A1})$$

$$\frac{d\chi}{d\tau} = \frac{\partial \hat{H}}{\partial \hat{P}_\chi} = \frac{1}{\gamma} \left\{ \frac{1}{k_w r} \left[\frac{\hat{P}_\chi}{k_w r} - a_w \left[1 + \frac{3k_w^2 r^2}{8} \right] \sin \chi \right] - \hat{P}_{z'} + \hat{P}_\chi \right\}, \quad (\text{A2})$$

$$\begin{aligned} \frac{d\hat{P}_r}{d\tau} = -\frac{\partial \hat{H}}{\partial(k_w r)} = \frac{1}{\gamma} \left\{ -\frac{a_w k_w r}{4} \left[\hat{P}_r + a_w \left[1 + \frac{k_w^2 r^2}{8} \right] \cos \chi \right] \cos \chi \right. \\ \left. + \left[\frac{\hat{P}_\chi}{k_w r} - a_w \left[1 + \frac{3k_w^2 r^2}{8} \right] \sin \chi \right] \left[\frac{\hat{P}_\chi}{k_w^2 r^2} + \frac{3a_w k_w r}{4} \sin \chi \right] \right\}, \quad (\text{A3}) \end{aligned}$$

$$\begin{aligned} \frac{d\hat{P}_\chi}{d\tau} = -\frac{\partial \hat{H}}{\partial \chi} = \frac{1}{\gamma} \left\{ a_w \left[1 + \frac{k_w^2 r^2}{8} \right] \left[\frac{\hat{P}_\chi}{k_w r} - a_w \left[1 + \frac{3k_w^2 r^2}{8} \right] \sin \chi \right] \sin \chi \right. \\ \left. + a_w \left[1 + \frac{3k_w^2 r^2}{8} \right] \left[\hat{P}_r + a_w \left[1 + \frac{k_w^2 r^2}{8} \right] \cos \chi \right] \cos \chi \right\}. \quad (\text{A4}) \end{aligned}$$

Here, $\tau = ck_w t$ and $\hat{H} = \gamma$. It is readily shown from Eqs. (A1)–(A4) that the steady-state solutions $(k_w r_0, \chi_0, \hat{P}_{r0}, \hat{P}_{\chi0})$ are given by

$$-a_w \left[\frac{3k_w r_0}{4} (1 + k_w^2 r_0^2) + \frac{1}{k_w r_0} \left[1 + \frac{3k_w^2 r_0^2}{8} \right] \right] \times \sin \chi_0 = \hat{P}_{z'}, \quad (\text{A5})$$

$$\cos \chi_0 = 0, \quad (\text{A6})$$

$$\hat{P}_{r0} = 0, \quad (\text{A7})$$

$$\hat{P}_{\chi0} = -(3a_w/4)k_w^3 r_0^3 \sin \chi_0, \quad (\text{A8})$$

which correspond to helical orbits with guiding center on the axis of the wiggler helix. Subtracting Eq. (A8) from Eq. (A5) yields the axial momentum

$$\hat{P}_{z0} = \hat{P}_{z'} - \hat{P}_{\chi0} = -a_w \left[\frac{1}{k_w r_0} + \frac{9k_w r_0}{8} \right] \sin \chi_0. \quad (\text{A9})$$

It is clear from Eq. (A9) that $\hat{P}_{z0} > 0$ when $\chi_0 = 3\pi/2$, and $\hat{P}_{z0} < 0$ when $\chi_0 = \pi/2$. Substituting Eqs. (A5)–(A8) into Eq. (69) gives¹³

$$\frac{\gamma^2 - 1}{a_w^2} = \left[1 + \frac{1}{k_w^2 r_0^2} \right] \left[1 + \frac{9k_w^2 r_0^2}{8} \right]^2. \quad (\text{A10})$$

Making use of Eq. (64) and $\gamma = \gamma_b$, it is readily shown that Eq. (A10) can be expressed as

$$\begin{aligned} \Delta = f(k_w r_0) \\ \cong 2^{-1/2} \left[\left[1 + \frac{1}{k_w^2 r_0^2} \right] \left[1 + \frac{9k_w^2 r_0^2}{8} \right]^2 - 1 \right]^{-1/2}, \quad (\text{A11}) \end{aligned}$$

which determines the gyroradius of the helical orbit. For $x > 0$, the function $f(x)$ is always non-negative and possesses the (single) maximum $f_m \cong 0.28$ at $x \cong 0.625$. Therefore Eq. (A11) has two real solutions for $0 \leq \Delta < f_m$.

- *Permanent address: Plasma Physics Laboratory, Princeton University, Princeton, NJ 08543.
- ¹A. J. Lichtenberg and M. A. Lieberman, *Regular and Stochastic Motion* (Springer-Verlag, New York, 1983).
- ²*Hamiltonian Dynamical Systems*, edited by R. S. MacKay and J. D. Meiss (Hilger, Philadelphia, 1987).
- ³M. V. Berry, in *Topics of Nonlinear Dynamics (La Jolla Institute)*, Proceedings of the Workshop on Topics in Nonlinear Dynamics, edited by S. Jorna, AIP Conf. Proc. No. 46 (AIP, New York, 1978), p. 16.
- ⁴V. I. Arnol'd, *Russ. Math. Surv.* **18**, 85 (1964).
- ⁵G. R. Smith and A. N. Kaufman, *Phys. Rev. Lett.* **34**, 1613 (1975); C. F. F. Karney and A. Bers, *ibid.* **39**, 550 (1977).
- ⁶F. Skiff, F. Anderegg, and M. Q. Tran, *Phys. Rev. Lett.* **58**, 1430 (1987).
- ⁷D. A. G. Deacon, L. R. Ellis, J. M. J. Madey, G. J. Ramian, H. A. Schwettman, and T. I. Smith, *Phys. Rev. Lett.* **38**, 892 (1977).
- ⁸*Free Electron Laser Handbook*, edited by W. Colson, C. Pellegrini, and A. Renieri (North-Holland, Amsterdam, 1989).
- ⁹C. W. Roberson and P. Sprangle, *Phys. Fluids B* **1**, 3 (1989).
- ¹⁰See, for example, R. C. Davidson and H. S. Uhm, *Phys. Fluids* **23**, 2076 (1980).
- ¹¹R. C. Davidson, *Physics of Nonneutral Plasmas* (Addison-Wesley, Reading, MA, 1990).
- ¹²L. Friedland, *Phys. Fluids* **23**, 2376 (1980).
- ¹³P. Diament, *Phys. Rev. A* **23**, 2537 (1981).
- ¹⁴R. K. Parker, R. H. Jackson, S. H. Gold, H. P. Freund, V. L. Granatstein, P. C. Efthimion, M. Herndon, and H. K. Kinkead, *Phys. Rev. Lett.* **48**, 238 (1982).
- ¹⁵H. P. Freund, *Phys. Rev. A* **27**, 1977 (1983); H. P. Freund and A. T. Drobot, *Phys. Fluids* **25**, 736 (1982); R. C. Davidson and H. S. Uhm, *J. Appl. Phys.* **53**, 2910 (1982).
- ¹⁶H. P. Freund, S. Johnston, and P. Sprangle, *IEEE J. Quantum Electron.* **QE-19**, 322 (1983); H. P. Freund and A. K. Ganguly, *ibid.* **QE-21**, 1073 (1985).
- ¹⁷J. A. Pasour, F. Mako, and C. W. Roberson, *J. Appl. Phys.* **53**, 7174 (1981).
- ¹⁸J. Fajans, D. A. Kirkpatrick, and G. Bekefi, *Phys. Rev. A* **32**, 3448 (1985).
- ¹⁹E. T. Scharlemann, *J. Appl. Phys.* **58**, 2154 (1985).
- ²⁰S. Riyopoulos and C. M. Tang, *Phys. Fluids* **31**, 1708 (1988).
- ²¹N. M. Kroll, P. L. Morton, and M. N. Rosenbluth, *IEEE J. Quantum Electron.* **QE-17**, 1436 (1981).
- ²²R. C. Davidson and J. S. Wurtele, *Phys. Fluids* **30**, 557 (1987); **30**, 2825 (1987).
- ²³C. Chen and G. Schmidt, *Comments Plasma Phys. Controlled Fusion* **12**, 83 (1988).
- ²⁴M. Billardon, *Phys. Rev. Lett.* **65**, 713 (1990).
- ²⁵C. Chen and R. C. Davidson, *Phys. Fluids B* **2**, 171 (1990).
- ²⁶C. Chen and R. C. Davidson, *Phys. Rev. A* **42**, 5041 (1990).